materials

Article

Diffusing Mn^{4+} into Dy^{3+} Doped $SrAl_2O_4$ for Full-Color Tunable Emissions

Bao-gai Zhai , Meng Meng Chen and Yuan Ming Huang *

School of Microelectronics and Control Engineering, Changzhou University, Changzhou 213164, China
* Correspondence: ymhuang@cczu.edu.cn

Abstract: Dy^{3+} and Mn^{4+} codoped $SrAl_2O_4$ ($SrAl_2O_4$:Dy^{3+},Mn^{4+}) phosphors were obtained by diffusing Mn^{4+} ions into Dy^{3+}-doped $SrAl_2O_4$ via the constant-source diffusion technique. The influences of diffusion temperature and diffusion time on the emissions of $SrAl_2O_4$:Dy^{3+},Mn^{4+} were investigated. It was found that: (i) efficient red emission peaking at 651 nm can be readily achieved for $SrAl_2O_4$:Dy^{3+} by simply diffusing Mn^{4+} into $SrAl_2O_4$:Dy^{3+} at 800 °C and above; (ii) the red emission of Mn^{4+} becomes dominant over the characteristic emissions of Dy^{3+} when the diffusion temperature is 900 °C or higher; and (iii) the intensity of the red emission of $SrAl_2O_4$:Dy^{3+},Mn^{4+} is far more sensitive to diffusion temperature than to diffusion time. Our results have demonstrated that full-color tunable emissions can be realized for $SrAl_2O_4$:Dy^{3+}, Mn^{4+} by tuning the parameters of diffusion temperature and diffusion time, which opens up a space for realizing easy color control of Dy^{3+}-doped inorganic materials.

Keywords: strontium aluminate; diffusion temperature; diffusion time; red emission of Mn^{4+}; photoluminescence

Citation: Zhai, B.-g.; Chen, M.M.; Huang, Y.M. Diffusing Mn^{4+} into Dy^{3+} Doped $SrAl_2O_4$ for Full-Color Tunable Emissions. *Materials* **2022**, *15*, 8170. https://doi.org/10.3390/ma15228170

Received: 30 September 2022
Accepted: 10 November 2022
Published: 17 November 2022

1. Introduction

Being a member of rare earth-activated luminescent materials, Dy^{3+}-doped $SrAl_2O_4$ ($SrAl_2O_4$:Dy^{3+}) has attracted much attention because of its interesting emission features [1–4]. Under ultraviolet excitation, the photoluminescence (PL) of $SrAl_2O_4$:Dy^{3+} is composed of two parts: (i) a broad emission band peaking at about 400 nm due to the intrinsic defects in $SrAl_2O_4$ [5]; and (ii) three narrow emission bands of Dy^{3+} activators centered at around 482, 574 nm and 663 nm, which are due to the optical transitions from $^4F_{9/2}$ to $^6H_{15/2}$, $^6H_{13/2}$, and $^6H_{11/2}$, respectively [6–11]. In principle, $SrAl_2O_4$:Dy^{3+} can be developed into a color-tunable light-emitting phosphor for applications in the solid state lighting industry because it contains blue, yellow, and red emissions. Unfortunately, the red emission band of Dy^{3+} is too weak to adjust the colorimetric performance of $SrAl_2O_4$:Dy^{3+}. Consequently, the realization of full-color emissions for $SrAl_2O_4$:Dy^{3+} seems to be an intractable problem unless a facile technique is developed to endow efficient red emissions to $SrAl_2O_4$:Dy^{3+}.

Red to deep red emission of Mn^{4+} ($3d^3$ electron configuration) provides a solution to this problem. The ground state ($^4A_{2g}$) and the lowest excited state (^2E_g) of Mn^{4+} arise from the t^3_{2g} configuration; the spin forbidden $^2E_g \rightarrow {}^4A_{2g}$ emission generally consists of a sharp line and associated vibronic sidebands. Under ultraviolet or blue irradiation, deep red emissions are observed for a number of Mn^{4+}-doped inorganic hosts [12,13]; examples include the red emissions for Mn^{4+}-doped $SrAl_2O_4$ (653 nm) [14], $Sr_4Al_{14}O_{25}$ (662 nm) [15], Mg_2TiO_4 (665 nm) [16,17], $CaAl_{12}O_{19}$ (656 nm) [18], and $CaAl_2O_4$ (658 nm) [19]. Thus, codoping $SrAl_2O_4$:Dy^{3+} with Mn^{4+} seems to be a promising strategy to realize full-color tunable emissions for $SrAl_2O_4$:Dy^{3+}. As documented in the literature, Chi et al. reported the red emission of Mn^{4+} in $SrAl_2O_4$ (around 660 nm) with a quenching concentration as low as 0.04 mol% [14]. Such a low quenching concentration poses stringent requirements on the doping technique, due to the fine control over the dose of Mn^{4+} in $SrAl_2O_4$:Dy^{3+},Mn^{4+}.

Making use of the advantages of the constant-source diffusion technique, our strategy in this work is to diffuse Mn^{4+} ions into $SrAl_2O_4:Dy^{3+}$ at low doping levels by tuning the parameters of diffusion temperature and diffusion time. Our results demonstrate that intense red emission peaking at 651 nm can be achieved by diffusing Mn^{4+} into $SrAl_2O_4:Dy^{3+}$ at 800ºC and higher, yielding full-color tunable emissions for Dy^{3+} and Mn^{4+} codoped $SrAl_2O_4$ ($SrAl_2O_4:Dy^{3+},Mn^{4+}$).

2. Experimental Section

2.1. Preparation of $SrAl_2O_4:Dy^{3+},Mn^{4+}$

The first step was to synthesize $SrAl_2O_4:Dy^{3+}$. Using the sol-gel combustion technique, $SrAl_2O_4:Dy^{3+}$ was synthesized by controlling the doping level of Dy^{3+} at 1.6 mol% [2–4]. Analytical grade reagents strontium nitrate ($Sr(NO_3)_2$), aluminum nitrate nonahydrate ($Al(NO_3)_3 \cdot 9H_2O$), urea, and boric acid (H_3BO_3) were purchased from a local chemical supplier, i.e., Sinopharm Chemical Reagents Co., Ltd. (Shanghai, China). Dysprosium oxide (Dy_2O_3) provided the source of Dy dopant, and the purity of Dy_2O_3 was 4 N. Under stirring with a magnetic bar, $Al(NO_3)_3 \cdot 9H_2O$ (0.4 mol), $Sr(NO_3)_2$ (0.2 mol), H_3BO_3 (0.02 mol), urea (6.0 mol), and Dy_2O_3 (0.0016 mol) were dissolved in 600 mL of deionized water. A transparent solution was obtained after the mixture was vigorously stirred for 4 h in a glass beaker. After being aged at room temperature for two weeks, the solution could be used for the sol-gel combustion. Urea and boric acid in the solution functioned as the fuel and flux, respectively. Alumina crucibles were utilized as the containers for the sol-gel combustion; the volume capacity of each alumina crucible was 50 mL. After being filled with 25 mL of the aged solution, the alumina crucible was transferred into a box furnace where the sol-gel combustion reaction took place. The temperature in the box furnace was kept at 700 °C before the solution-containing crucible was added. During the combustion, the temperature in the furnace was elevated to about 820 °C, but the temperature in the flame could reach 1300 °C. After the sol-gel combustion, white powders were collected. According to the molar ratio of Dy^{3+} ions to Sr^{2+} ions in the solution, the nominal doping concentration of Dy^{3+} in $SrAl_2O_4$ was determined to be 1.6 mol%.

The second step was to yield $SrAl_2O_4:Dy^{3+},Mn^{4+}$ by diffusing Mn^{4+} into $SrAl_2O_4:Dy^{3+}$ via the constant-source diffusion technique. Cylindrical corundum crucibles (ϕ40 mm) with a height of 35 mm were employed as the vessel for diffusion. A thin layer of MnO_2 (about 1 μm in thickness) was deposited onto the bottom of the crucible for constant-source diffusion. $SrAl_2O_4:Dy^{3+}$ powders were stored in the MnO_2-coated crucible, which was transferred into an air filled tubular furnace for Mn^{4+} diffusion. The diffusion was carried out under air atmosphere. The doses of Mn^{4+} in $SrAl_2O_4:Dy^{3+},Mn^{4+}$ were controlled by tuning the diffusion temperature and diffusion time.

2.2. Phase, Morphology, and Elemental Composition of $SrAl_2O_4:Dy^{3+},Mn^{4+}$

The phase of $SrAl_2O_4:Dy^{3+},Mn^{4+}$ phosphors was determined by their X-ray diffraction (XRD) profiles. The XRD profiles of $SrAl_2O_4:Dy^{3+},Mn^{4+}$ phosphors were recorded on an X-ray diffractometer (D/max 2500 PC, Rigaku Corporation, Akishima, Japan). The wavelength of the Cu Kα radiation was 0.15405 nm. The morphology of $SrAl_2O_4:Dy^{3+},Mn^{4+}$ phosphors was characterized with a scanning electron microscope (SEM) (model S-4800, Hitachi, Tokyo, Japan). The elemental composition of $SrAl_2O_4:Dy^{3+},Mn^{4+}$ phosphors was provided by the energy dispersive X-ray (EDX) spectrum of the synthesized phosphor. The nanostructures and crystal lattice of $SrAl_2O_4:Dy^{3+},Mn^{4+}$ were investigated on a transmission electron microscope (TEM) (model JEOL JEM-2100, Japan Electronics Corp, Akishima, Japan). Samples for TEM analysis were prepared by dispersing the particles of the phosphor in ethanol. After being excited in an ultrasonic cleaner for 10 min, a drop of the suspension was dried on a carbon-coated copper grid.

To determine the valence states of dopants Mn^{4+} and Dy^{3+} in $SrAl_2O_4:Dy^{3+},Mn^{4+}$, we performed X-ray photoelectron spectroscopy (XPS) analysis on an Escalab 250Xi spectrophotometer (Thermo Scientific, Waltham, MA, USA). Coming from Al Kα radiation, the energy of the incident X-ray was 1486.6 eV for the XPS characterization. Samples were not cleaned and not sputtered before XPS characterization. All the samples were analyzed by the charge correction. The binding energy of the standard C–C bond of the calibrated XPS instrument was 284.8 eV.

2.3. PL Spectra of $SrAl_2O_4$:Dy^{3+},Mn^{4+}

The steady-state PL spectra of $SrAl_2O_4$:Dy^{3+},Mn^{4+} phosphors were acquired with a spectrophotometer (Tianjin Gangdong Ltd., Tianjin, China). A helium-cadmium laser (Kimmon Electric Co., Ltd., Tokyo, Japan) provided the excitation source for the PL measurement. The emission wavelength of the laser radiation was 325 nm; the output power of the laser radiation was 13 mW. Each PL spectrum was taken at room temperature.

2.4. PL Decay Curves of $SrAl_2O_4$:Dy^{3+},Mn^{4+}

On a picosecond fluorescence lifetime spectrometer (LifeSpec II, Edinburgh Instruments, Edinburgh, UK), the PL decay curves of intrinsic defect-related emissions of $SrAl_2O_4$:Dy^{3+} before Mn^{4+} diffusion were measured at room temperature. The time correlated single photon counting technique was applied in the photon detection. A picosecond pulsed light-emitting diode provided the pulsed excitation. The excitation wavelength of the pulsed laser was 320 nm. The pulse width of the picosecond pulsed light-emitting diode was about 860 ps. For the PL decay curve, the detection wavelength was 400 nm, and the pulse repetition rate of the light source was fixed at 10 MHz, corresponding to a pulse every 100 ns. Details on the PL decay characterization could be found elsewhere [20,21]. In contrast, the PL decay curve of the $SrAl_2O_4$:Dy^{3+} after Mn^{4+} diffusion was measured at room temperature on a transient-state fluorescence spectrometer (FS5, Edinburgh Instruments, Edinburgh, UK). The PL decay curve of Mn^{4+} emission was recorded at 651 nm for $SrAl_2O_4$:Dy^{3+} after Mn^{4+} diffusion at 1000 °C. A pulsed Xenon lamp was employed to provide the pulsed excitation.

3. Results and Discussions

3.1. Phase and Morphology of $SrAl_2O_4$:Dy^{3+},Mn^{4+}

Figure 1 represents the X-ray diffraction (XRD) curves of $SrAl_2O_4$:Dy^{3+} before Mn^{4+} diffusion (*a*) and after Mn^{4+} diffusion at temperatures of 600 °C (*b*), 700 °C (*c*), 800 °C (*d*), 900 °C (*e*), and 1000 °C (*f*). The duration of each diffusion was 4 h. The diffraction data of standard monoclinic $SrAl_2O_4$ (JCPDS card no. 34-0379) are shown at the bottom of Figure 1 for comparison. Evidently, pure phase $SrAl_2O_4$ is formed when the diffusion temperatures are 900 and 1000 °C [2–5]. In contrast, a secondary phase is formed in $SrAl_2O_4$ before Mn^{4+} diffusion (curve *a*) and after Mn^{4+} diffusion at 600, 700, and 800 °C (curves *b*–*d*), due to the presence of a diffraction peak at $2\theta = 25°$. This phenomenon can be attributed to the formation of an aluminoborate complex in the combustion synthesis due to the addition of boric acid. Boric acid, which is used as a fluxing agent in promoting the formation of the required crystalline phase, can also behave as one of the precursor materials for the formation of aluminoborate complexes. The formed aluminoborate complexes can be decomposed and evaporated after annealing at high temperatures. This is the reason why the diffraction peak at $2\theta = 25°$ gradually loses its intensity when the diffusion temperature is elevated from 600 to 800 °C.

Monoclinic $SrAl_2O_4$ has a stuffed tridymite structure with the space group $P2_1$ and $Z = 4$. As described in our previous work, monoclinic $SrAl_2O_4$ has a three-dimensional network of corner-sharing $[AlO_4]$ tetrahedra with channels present in the *a*- and *c*-directions. Two crystallographically different Sr^{2+} sites are present in the unit cell of $SrAl_2O_4$, and these Sr^{2+} ions are located along the channels [5]. Therefore, it is easy for Dy^{3+} and Mn^{4+} to dope $SrAl_2O_4$. Depending on their coordination numbers (CN), the effective ionic radii of cations vary to some extent. In the case of site occupancy, the effective ionic radii of Sr^{2+}, Dy^{3+}, Al^{3+}, and Mn^{4+} are 0.145 (CN = 9), 0.122 (CN = 9), 0.053 (CN = 4), and 0.053 nm

(CN = 4), respectively [22]. Due to their comparable ionic sizes, dopants Dy^{3+} and Mn^{4+} tend to replace the Sr^{2+} and Al^{3+} sites in the lattice of $SrAl_2O_4$, respectively.

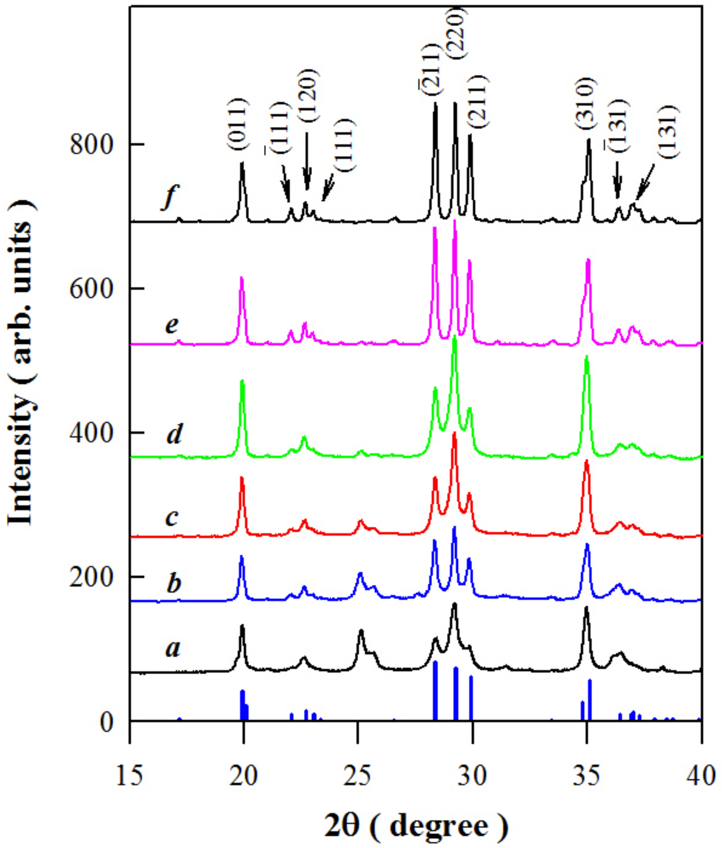

Figure 1. XRD curves of the $SrAl_2O_4$:Dy^{3+} before Mn^{4+} diffusion (*a*) and after Mn^{4+} diffusion at temperatures of 600 °C (*b*), 700 °C (*c*), 800 °C (*d*), 900 °C (*e*), and 1000 °C (*f*). The duration of each diffusion is 4 h. The doping concentration of Dy^{3+} is 1.6 mol%. The standard diffraction data of monoclinic $SrAl_2O_4$ (JCPDS card no. 34-0379) are shown at the bottom of the figure as vertical bars for comparison.

Figure 2 displays the SEM micrograph (a), low-magnification TEM micrograph (b), and high-resolution TEM micrograph (c) of $SrAl_2O_4$:Dy^{3+} after Mn^{4+} diffusion at 800 °C for 4 h. As shown in Figure 2a, some of the particles are as small as 20 nm in diameter, but they are prone to forming large aggregates because of their high surface energy. As shown in Figure 2b, the aggregate consists of a large number of nanoparticles with their dimensions up to 80 nm. Our previous work has evidenced the formation of a number of $SrAl_2O_4$ nanocrystals in a single aggregate [5]. The high-resolution TEM micrograph in Figure 2c illustrates the crystal lattices of one $SrAl_2O_4$:Dy^{3+},Mn^{4+} nanoparticle. The spacing between two adjacent planes in Figure 2c is found to be 0.314 nm, which is in good agreement with the distance between two adjacent ($\bar{2}11$) crystallographic planes of monoclinic $SrAl_2O_4$. Thus, the micrographs in Figure 2 demonstrate that the synthesized $SrAl_2O_4$:Dy^{3+}, Mn^{4+} exhibits good crystallinity.

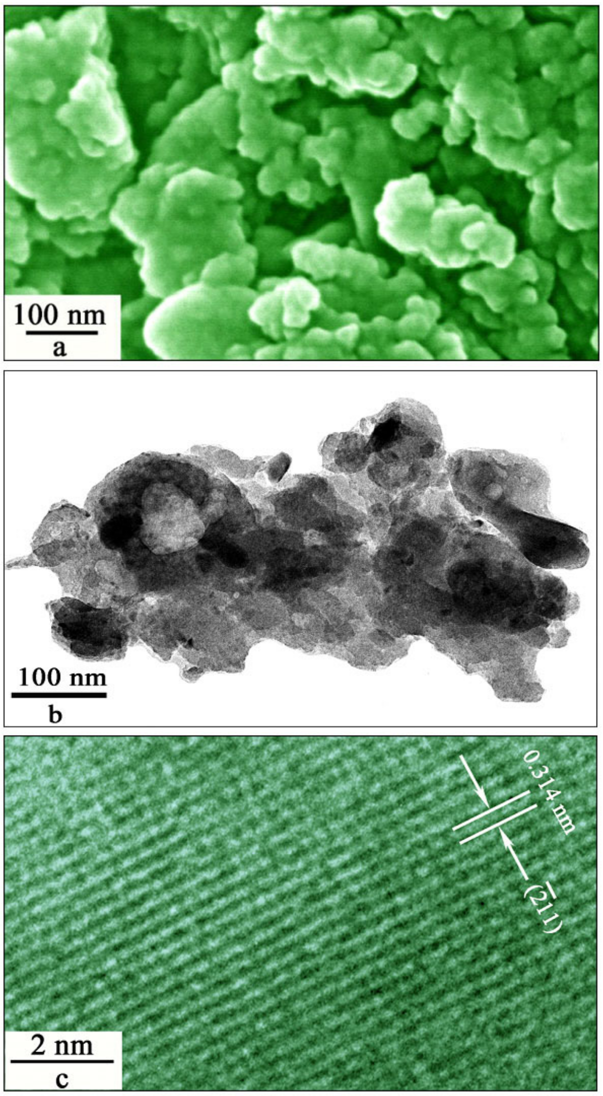

Figure 2. SEM micrograph (**a**), low-resolution TEM micrograph (**b**), high-resolution TEM micrograph (**c**) of $SrAl_2O_4$:Dy^{3+} after Mn^{4+} diffusion at 800 °C for 4 h. The doping concentration of Dy^{3+} is 1.6 mol%.

3.2. *EDX Spectrum of $SrAl_2O_4$:Dy^{3+},Mn^{4+}*

Figure 3 illustrates the EDX spectrum of $SrAl_2O_4$:Dy^{3+} after Mn^{4+} diffusion at 800 °C for 4 h. As mentioned in the experimental section, the doping concentration of Dy^{3+} is 1.6 mol%. As can be seen in Figure 3, the characteristic X-ray emissions of O(Kα), Al(Kα), and Sr(Lα_1) are located at 0.525, 1.486, and 1.806 keV, respectively. In the meantime, the characteristic emissions of Dy(Lα_1) and Dy(Lβ_1) can be identified at 6.495 and 7.248 keV, respectively. Additionally, the X-ray emissions of Au(Mα_1) and Au(Lα_1) are located at 2.122 and 9.713 keV, respectively. However, element Mn is not detected with the EDX because the doping concentration is very low, which is outside the detection limit of the EDX facility. The detection limit of our EDX is about 1 wt. % for element Mn. As previously described, the Au element in the specimen is introduced in the process of Au sputtering for the convenience of SEM characterization. As expected, the EDX spectrum of $SrAl_2O_4$:Dy^{3+},Mn^{4+} verifies the presence of elements Al, Sr, O, and Dy in the phosphor.

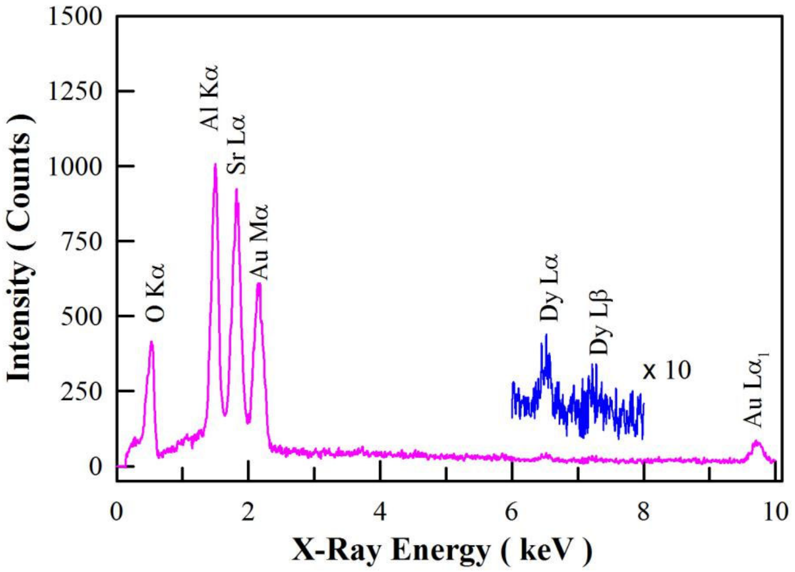

Figure 3. EDX spectrum of $SrAl_2O_4:Dy^{3+}$ (1.6 mol%) after Mn^{4+} diffusion at 800 °C for 4 h.

3.3. XPS Spectrum of $SrAl_2O_4:Dy^{3+},Mn^{4+}$

The oxidation states of Mn and Dy in $SrAl_2O_4:Dy^{3+},Mn^{4+}$ are examined with the XPS analysis. Figure 4 represents the high-resolution XPS spectra of Mn 2p (a) and Dy 3d (b) in $SrAl_2O_4:Dy^{3+},Mn^{4+}$. Mn^{4+} ions are diffused into $SrAl_2O_4:Dy^{3+}$ at 900 °C for 4 h. As can be seen in Figure 4a, the peaks of Mn $2p_{3/2}$ and Mn $2p_{1/2}$ are located at about 642.2 and 653.8 eV, respectively. These binding energies indicate that the oxidation state of Mn ion is 4+. Figure 4b demonstrates that the peaks of the spin-orbit component ($3d_{5/2}$ and $3d_{3/2}$) of Dy^{3+} are located at approximately 1297.6 and 1335.1 eV, respectively. The high-resolution XPS spectrum of O 1s in $SrAl_2O_4:Dy^{3+},Mn^{4+}$ nanocrystals is shown in Figure S1. Peaking at 531.78 eV, the XPS spectral profile of O1s can be deconvoluted into several components.

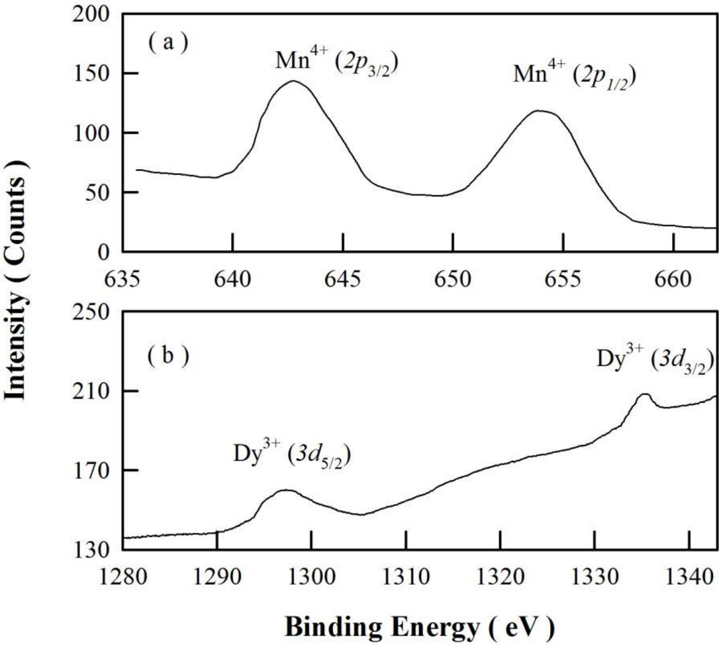

Figure 4. High-resolution XPS spectra of Mn 2p (**a**) and Dy 3d (**b**) in $SrAl_2O_4:Dy^{3+}$ after Mn^{4+} diffusion at 900 °C for 4 h.

3.4. PL Spectra of $SrAl_2O_4:Dy^{3+}$ after Mn^{4+} Diffusion at Different Temperatures

Figure 5 represents the PL spectra of $SrAl_2O_4:Dy^{3+}$ before Mn^{4+} diffusion (a) and after Mn^{4+} diffusion at 600 °C (b), 700 °C (c), 800 °C (d), 900 °C (e), and 1000 °C (f). The diffusion time is 4 h for each sample. As can be seen in Figure 5a, the PL spectrum of the $SrAl_2O_4:Dy^{3+}$ before Mn^{4+} diffusion consists of a broad PL band peaking at about 400 nm, and two characteristic emission bands of Dy^{3+} ions peaking at 482 and 572 nm, respectively. The broad emission band of $SrAl_2O_4:Dy^{3+}$ comes from intrinsic defects (namely oxygen and/or strontium vacancies) in the lattice of $SrAl_2O_4$ [5]. The narrow emission bands peaking at 482 and 572 nm are due to the $^4F_{9/2} \rightarrow {}^6H_{15/2}$ and $^4F_{9/2} \rightarrow {}^6H_{13/2}$ transitions of Dy^{3+} [2–4,6]. Before Mn^{4+} diffusion, the broad emission band of $SrAl_2O_4:Dy^{3+}$ is very strong. Conversely, the two narrow emission bands centered at 482 and 572 nm are very weak. No red emission can be detected in the range of 600–700 nm for $SrAl_2O_4:Dy^{3+}$ before Mn^{4+} diffusion. Thus, the perception color of the emissions of $SrAl_2O_4:Dy^{3+}$ before Mn^{4+} diffusion is blue (Figure S2). Actually, quite similar intrinsic defect-related emissions have been recorded for a large number of aluminates, such as undoped $CaAl_2O_4$ [20,23], Dy^{3+}-doped $BaAl_2O_4$ [21], Tb^{3+}-doped $CaAl_2O_4$ [24], and Tb^{3+}-doped $SrAl_2O_4$ [25]. At high annealing temperatures, oxygen atoms in air can migrate into the crystal lattice to repair the defects with the result of a decline in the population density of oxygen vacancies in $SrAl_2O_4:Dy^{3+}$. Therefore, the intrinsic defect-related emissions should be weakened or even have disappeared after air annealing at high temperatures. Indeed, the broad emission band of $SrAl_2O_4:Dy^{3+}$ disappears when the diffusion temperature is elevated to 600 °C and higher, as shown in Figure 5b–f.

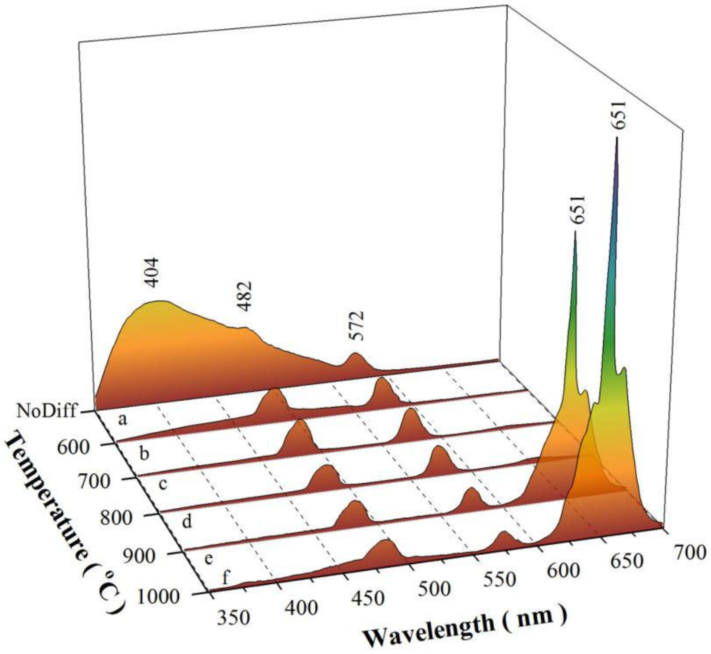

Figure 5. PL spectra of $SrAl_2O_4:Dy^{3+}$ before Mn^{4+} diffusion (a) and after Mn^{4+} diffusion at 600 °C (b), 700 °C (c), 800 °C (d), 900 °C (e), and 1000 °C (f). The duration of each diffusion is 4 h.

The most striking feature in Figure 5 is that the red emission peaking at 651 nm gradually gains intensity as the diffusion temperature increases from 600 to 1000 °C. Figure S3 illustrates the PL spectra of $SrAl_2O_4:Dy^{3+}$ after Mn^{4+} diffusion at 800 °C (a), 900 °C (b), and 1000 °C (c) for 4 h. The inset in Figure S3 shows the zoomed section of the PL spectra of $SrAl_2O_4:Dy^{3+},Mn^{4+}$ in the range of 620–700 nm. Quantitative analysis shows that the intensities of the red PL band are about 3%, 9%, and 30% that of the narrow blue PL band of Dy^{3+}, peaking at 482 nm when $SrAl_2O_4:Dy^{3+}$ is subject to Mn^{4+} diffusion at 600, 700, and 800 °C, respectively. Surprisingly, the red PL band of $SrAl_2O_4:Dy^{3+},Mn^{4+}$ becomes dominant in intensity when the diffusion temperature is beyond 800 °C. As shown by the

PL spectra *e* and *f* in Figure 5, the peak of the red PL band is located at 651 nm, which is in good agreement with the deep red emission of Mn^{4+}-doped $SrAl_2O_4$ [14]. The integrated PL intensities of the red emission in PL spectra *e* and *f* are about 11.7 and 20.9 fold stronger than that of the narrow blue PL band of Dy^{3+} peaking at 482 nm. Thus, the PL spectra *e* and *f* verify that strong red emission can be achieved via Mn^{4+} diffusion into $SrAl_2O_4$:Dy^{3+} at diffusion temperatures higher than 800 °C. The PL quantum efficiency is a key parameter for the quantification of luminescent processes in phosphors. Characterized by Quantaurus-QY (Hamamatsu, Japan), the PL quantum yield values of these compounds are found to vary in the range of 27–60%, depending on the diffusion temperature and the diffusion time. The PL quantum yield values of commercial phosphors are higher than 75%. For example, the PL quantum yield of $Y_3Al_5O_{12}$:Ce^{3+} is known to be around 97%, and the green silicate Ba_2SiO_4:Eu^{2+} shows a PL quantum yield of about 79%. Compared to the high PL quantum yield values of these commercial phosphors, the PL quantum yield values of $SrAl_2O_4$:Dy^{3+},Mn^{4+} are quite low.

Once Mn^{4+} is diffused into $SrAl_2O_4$:Dy^{3+}, a set of energy levels are introduced into the bandgap of $SrAl_2O_4$. As documented in the literature, the ground state and the excited state of Mn^{4+} can be denoted as ^2E_g and $^4A_{2g}$, respectively [15], and the red emission peaking at 651 nm is associated with the $^2E_g \rightarrow {}^4A_{2g}$ transition of Mn^{4+}. One might wonder how it would be possible to make the red emission much stronger than the characteristic emissions of Dy^{3+} in $SrAl_2O_4$:Dy^{3+},Mn^{4+}. The answer lies in the much higher dose of Mn^{4+} in $SrAl_2O_4$:Dy^{3+},Mn^4 at higher diffusion temperatures. The diffusion coefficient is known to depend on temperature. The diffusion coefficient in solids at different temperatures is found to be well predicted by the Arrhenius equation:

$$D = D_0 \exp\left(-\frac{E_A}{kT}\right) \tag{1}$$

where E_A is the activation energy for diffusion (in eV), D_0 is the diffusion coefficient at infinite temperature (in cm^2/s), D is the diffusion coefficient (in cm^2/s), k is the Boltzmann constant, T is the absolute temperature (in K). The dose, which is the total amount of a dopant diffused into a solid, of a constant-source diffusion can be expressed as:

$$Q = \frac{2N_0}{\sqrt{\pi}}\sqrt{Dt} \tag{2}$$

where Q is the dose in the host (atoms/cm), N_0 is the surface concentration (atoms/cm^2), D is the diffusion coefficient (cm^2/s), and t is the diffusion time (s). In the constant source diffusion, the dose increases as a function of diffusion temperature and diffusion time. Equations (1) and (2) predict that the dose quickly increases with the diffusion temperature for given values of E_A and t. The activation energy for Mn^{4+} diffusion in $SrA_{12}O_4$ has not yet been reported. An estimation of the activation energy for Mn^{4+} diffusion in $SrAl_2O_4$ becomes a choice. As documented in the literature, de Biasi and Grillo reported that the activation energies of 266 kJ/mol (2.76 eV) for the diffusion of Mn^{2+} in CaO and 203 kJ/mol (2.10 eV) for the diffusion of Mn^{2+} in MgO [26]. Additionally, Portavoce et al. reported that the activation energy for Mn in monocrystalline Ge is 2.37 eV [27]. After having considered the typical activation energies of As in polysilicon (3.9 eV), B in polysilicon (2.4–2.5 eV), B in SiO_2 (2.38–3.53 eV), Ga in SiO_2 (4.17 eV), and As in SiO_2 (3.7–4.7 eV), it seems reasonable to assume that the activation energy for Mn^{4+} diffusion in $SrAl_2O_4$ is in the range of 2–5 eV. Assuming that E_A takes the value of 3.0 eV, the doses of Mn^{4+} diffused into $SrAl_2O_4$ at 700, 800, 900, and 1000 °C are 7.8, 41, 163, and 523 times as large, respectively, as the dose of Mn^{4+} diffused into $SrAl_2O_4$ at 600 °C (Figure S4). The quick increase in the dose of Mn^{4+} at high diffusion temperature makes the red emission of Mn^{4+} dominant over the characteristic emissions of Dy^{3+} in $SrAl_2O_4$:Dy^{3+},Mn^4. As a result, full-color tunable emissions are realized for $SrAl_2O_4$:Dy^{3+},Mn^4 due to the complementary red emission of Mn^{4+}. Rather than doping the host with red-emitting rare earth ions, such as Eu^{3+} ($^5D_0 \rightarrow ^7F_2$ at 612 nm) [11,28], Sm^{3+} ($^4G_{5/2} \rightarrow ^6H_{7/2}$ at 605 nm) [29], or Pr^{3+} ($^3P_1 \rightarrow ^3F_3$ at 642 nm) [30], diffusing Mn^{4+} into $SrAl_2O_4$:Dy^{3+} makes the red emission cost effective.

3.5. Emission Colors of $SrAl_2O_4$:Dy^{3+},Mn^{4+}

Along with the characteristic emissions of Dy^{3+} peaking at 482 nm (blue) and 572 nm (yellow), the emergence of the red emission of Mn^{4+} makes $SrAl_2O_4$:Dy^{3+},Mn^{4+} suitable for multi-color emissions. Color coordinates, which are important parameters to quantitatively describe the emission color for luminescent materials, can be calculated from their PL spectral data [31,32]. Figure 6 shows photographs of the light-emitting $SrAl_2O_4$:Dy^{3+} before Mn^{4+} diffusion (a) and after Mn^{4+} diffusion at 600 °C (b), 700 °C (c), 800 °C (d), 900 °C (e), and 1000 °C (f). The chromaticity coordinates are marked onto the corresponding photographs. Before Mn^{4+} diffusion, the PL color is blue with the chromaticity coordinates of (0.174, 0.157) for $SrAl_2O_4$:Dy^{3+}, as shown in Figure 6a. When the diffusion temperature arises from 600 to 800 °C, the emission color of $SrAl_2O_4$:Dy^{3+},Mn^{4+} evolves from bluish green to white due to the weakened blue emission of the host at high diffusion temperature, as shown in Figure 6b–d. Interestingly, the emission color dramatically changes when $SrAl_2O_4$:Dy^{3+} is subject to Mn^{4+} diffusion at a temperature higher than 800 °C. As illustrated in Figure 6e,f, the emission colors of $SrAl_2O_4$:Dy^{3+},Mn^{4+} are pink and purplish red when the diffusion temperatures are 900 and 1000 °C, respectively. The dramatic changes in emission color are due to the enhanced red emission of Mn^{4+}. The CIE chromaticity diagram of the emissions of $SrAl_2O_4$:Dy^{3+} before Mn^{4+} diffusion (a) and after Mn^{4+} diffusion at temperatures of 600 °C (b), 700 °C (c), 800 °C (d), 900 °C (e), and 1000 °C (f) is shown in Figure S5. It is clear that full-color tunable emissions can be achieved for $SrAl_2O_4$:Dy^{3+},Mn^{4+} by tuning the diffusion temperature of Mn^{4+}.

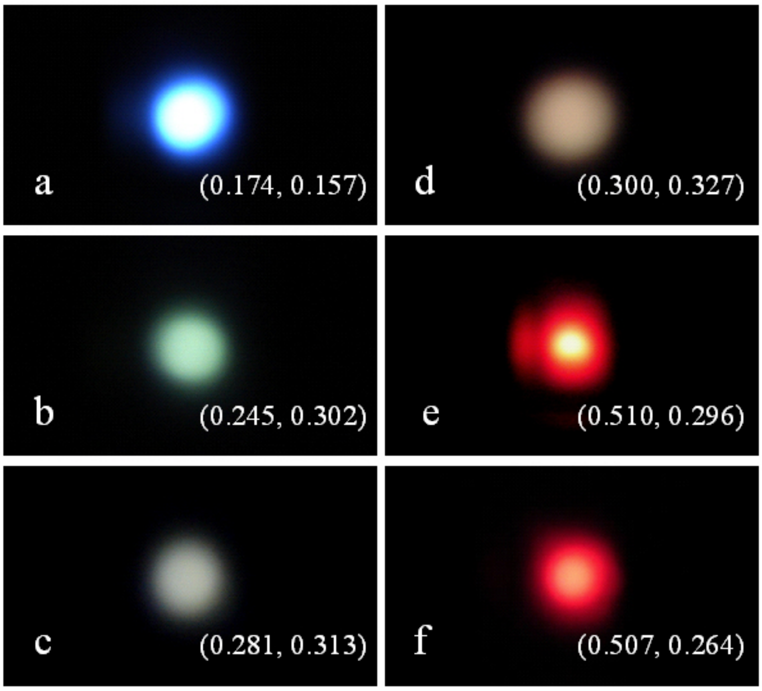

Figure 6. Photographs of the PL from $SrAl_2O_4$:Dy^{3+} before Mn^{4+} diffusion (**a**) and after Mn^{4+} diffusion at temperatures of 600 °C (**b**), 700 °C (**c**), 800 °C (**d**), 900 °C (**e**), and 1000 °C (**f**). The diffusion time is 4 h.

3.6. PL Spectra of $SrAl_2O_4$:Dy^{3+} after Mn^{4+} Diffusion for Different Times

According to Equation (2), the dose of the constant-source diffusion increases with the diffusion time when the diffusion temperature is fixed. Therefore, the dose of Mn^{4+} in $SrAl_2O_4$:Dy^{3+},Mn^{4+} can be tuned by the diffusion time. Figure 7 depicts the PL spectra of $SrAl_2O_4$:Dy^{3+} after Mn^{4+} diffusion at 800 °C for different times: 4 h, 8 h, 12 h, 16 h, 20 h, and 24 h. It can be seen in Figure 7 that each PL spectrum consists of one blue emission band centered at 482 nm, one yellow emission band centered at 572 nm, and one red band peaking at about 651 nm. Obviously, the sharp emission peak at 651 nm can be ascribed to the $^2E_g \rightarrow {}^4A_{2g}$ transition of tetrahedrally-coordinated Mn^{4+} [16]. The quenching concentration of Mn^{4+} in $SrAl_2O_4$ was reported to be 0.04 mol% [14]. The red emission in Figure 7 increases slowly with the diffusion time, indicating that the concentration of Mn^{4+} in $SrAl_2O_4$:Dy^{3+},Mn^{4+} can be well controlled before reaching the quenching concentration. According to Equation (2), the doses of Mn^{4+} diffused into $SrAl_2O_4$:Dy^{3+} at 800 °C for 8, 12, 16, 20, and 24 h are 1.4, 1.7, 2.0, 2.2, and 2.5 times as large as the dose of Mn^{4+} diffused into $SrAl_2O_4$:Dy^{3+} at 800 °C for 4 h. Thus, it is understandable that the diffusion temperature, rather than the diffusion time, is more effective in enhancing the red emission of $SrAl_2O_4$:Dy^{3+},Mn^{4+}. Obviously, diffusing Mn^{4+} into $SrAl_2O_4$:Dy^{3+} by the constant-source diffusion technique exhibits advantages because tuning the parameters of diffusion temperature and diffusion time can finely control the doping concentration at low doping levels.

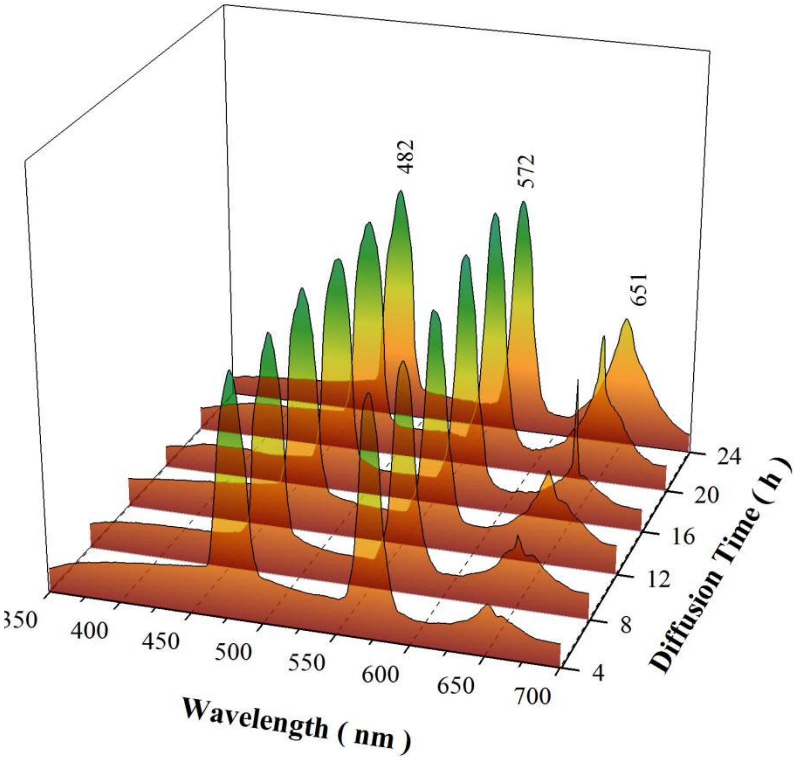

Figure 7. PL spectra of $SrAl_2O_4$:Dy^{3+} (1.6 mol%) after Mn^{4+} diffusion at 800 °C for different times: 4 h, 8 h, 12 h, 16 h, 20 h, and 24 h.

Thermal diffusion of Mn^{4+} into $SrAl_2O_4$:Dy^{3+} has potential industrial sense because it modifies the PL properties of $SrAl_2O_4$:Dy^{3+} phosphor with the introduction of red emissions of Mn^{4+} ions. The diffusion time of 4 h seems quite long when compared to the diffusion times of B and P doping silicon in advanced semiconductor fabrication sectors. Optimizing the diffusion time and diffusion temperature is a key procedure for the application of $SrAl_2O_4$:Dy^{3+},Mn^{4+} as phosphors in the solid state lighting industry.

3.7. PL Decays of $SrAl_2O_4$:Dy^{3+},Mn^{4+}

Figure 8a represents the PL decay curve of $SrAl_2O_4$:Dy^{3+} before Mn^{4+} diffusion. The excitation wavelength for this decay curve is 320; the detection wavelength is 400 nm. The instrument response function is shown in Figure 8a (in blue) for the decay curve. The exponential reconvolution of the raw data is represented by the green solid curve in Figure 8a. Our analysis reveals that this PL decay curve can be best described by a triexponential decay model with three largely different time constants. The fitting parameters of the PL decay are listed in Figure 8a. On one hand, the three time constants are largely different, suggesting the presence of three distinctly different channels in the phosphor for radiative recombination. On the other hand, the averaged lifetime of the PL decay is 4.78 ns, which provides complementary information about the intrinsic defect-related emissions of $SrAl_2O_4$.

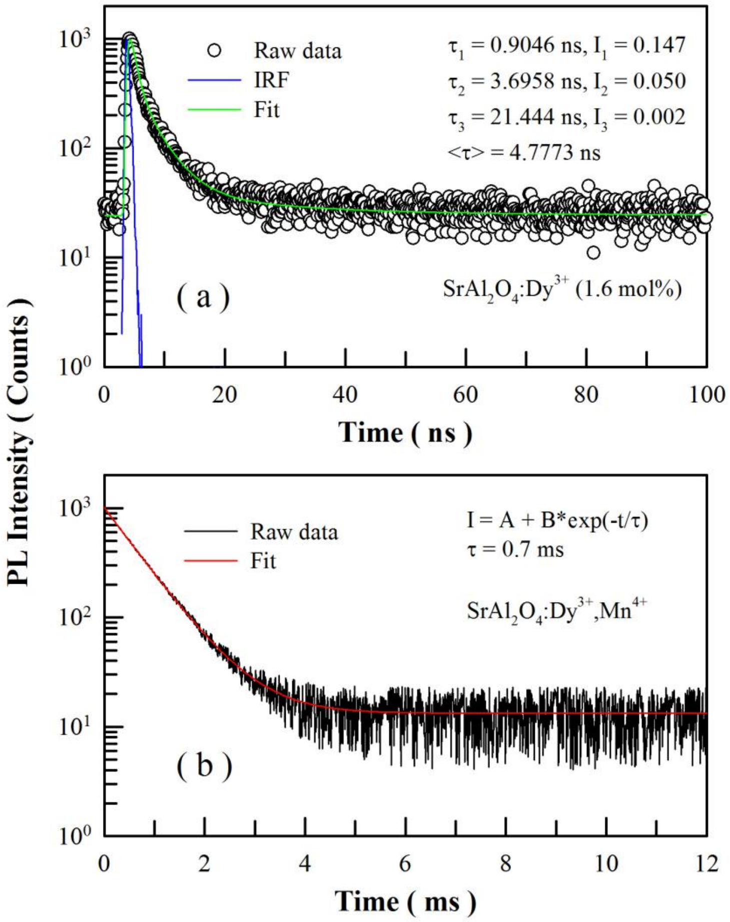

Figure 8. (**a**) PL decay curve of $SrAl_2O_4:Dy^{3+}$ before Mn^{4+} diffusion; the detection wavelengths is 400 nm. (**b**) PL decay curve of $CaAl_2O_4:Dy^{3+}$ after Mn^{4+} diffusion at 1000 °C for 4 h; the detection wavelength is 651 nm. The excitation wavelength is 320 nm.

Figure 8b represents the PL decay of $SrAl_2O_4:Dy^{3+}$ after Mn^{4+} diffusion at 1000 °C for 4 h. The excitation wavelength for this decay curve is 320; the detection wavelength is 651 nm. The exponential reconvolution of the raw data in Figure 8b is represented by the red solid curve. Clearly, the PL decay curve in Figure 8b is well described by a mono-exponential decay model with a time constant of 0.7 ms. As documented in the literature, Cao et al. reported that the lifetime of Mn^{4+} emission in Mn^{4+}-doped $CaAl_2O_4$ decreased from 1.35 to 0.94 ms as the concentration of Mn^{4+} increased from 0.2 to 1.6 mol% [19]. Sun et al. reported that the lifetime of Mn^{4+} emissions in Mn^{4+}-doped Ba_2GdTaO_6 was around 0.3 ms [33]. Apparently, the PL lifetime of Mn^{4+} emissions in $SrAl_2O_4:Dy^{3+},Mn^{4+}$ is in line with those of Mn^{4+} emissions in a large number of Mn^{4+}-doped inorganic materials [19,33–36]. The lifetime of Mn^{4+} emission of $SrAl_2O_4:Dy^{3+},Mn^{4+}$ is about five orders of magnitude higher than that of the intrinsic defect-related emissions of $SrAl_2O_4:Dy^{3+}$, meaning that the red emission is caused by the parity-forbidden d-d transitions of the Mn^{4+} ions.

The PL decay time of the defect-related blue emission band is 4.78 ns, which is unusually fast when compared to the PL decay time of the defect-related emission in some complex oxides, such as tungstates and molybdates. For example, the PL decay times of $PbMoO_4$ and $ZnWO_4$ crystals are of the order of tens and hundreds of microseconds [37]. We tried to measure the decay of this broad blue band in microsecond or even millisecond scales, but no obvious changes in the PL decay time were found for our sol-gel-derived $SrAl_2O_4$:Dy^{3+},Mn^{4+} when the time scales of the PL decay measurements were extended to 200, 500, 1000, 2000, 5000, and 50,000 ns, respectively. It is known the PL decay time of a phosphor depends on the non-radiative recombination rates in the phosphor. The higher the non-radiative recombination rate, the shorter the PL decay time will be. When compared to $PbMoO_4$ and $ZnWO_4$ single crystals, the sol-gel-derived $SrAl_2O_4$:Dy^{3+},Mn^{4+} nanocrystals have a much higher density of oxygen vacancies, which in turn enhances the non-radiative recombination rate. Therefore, the high density of oxygen vacancies in the sol-gel-derived $SrAl_2O_4$:Dy^{3+},Mn^{4+} nanocrystals is responsible for the short PL decay time. Such an interpretation is supported by the averaged PL decay times of several nanoseconds for $ZnWO_4$ nanocrystals [38,39], $ZnMoO_4$ nanocrystals [40], zinc molybdenum oxide hydrate nanocrystals [41], and pentazinc dimolybdate pentahydrate [42]. In particular, our previous work revealed that the averaged PL decay time of $ZnWO_4$ nanocrystals can be extended from 2.25 to 1770 ns when the population density of oxygen vacancies in $ZnWO_4$ nanocrystals is decreased via thermal annealing in air [43].

4. Conclusions

Employing a constant-source diffusion technique, $SrAl_2O_4$:Dy^{3+},Mn^{4+} phosphors were obtained by diffusing Mn^{4+} ions into $SrAl_2O_4$:Dy^{3+}. The influences of diffusion temperature and diffusion time on the red emission were investigated. It was found that: (i) peaking at 651 nm, the red emission of $SrAl_2O_4$:Dy^{3+},Mn^{4+} became dominant over the characteristic emissions of Dy^{3+} when the diffusion temperature was higher than 800 °C; (ii) the red emission intensity of $SrAl_2O_4$:Dy^{3+},Mn^{4+} was far more sensitive to diffusion temperature than to diffusion time; and (iii) full-color tunable emissions were realized for $SrAl_2O_4$:Dy^{3+},Mn^{4+} by constant source diffusion. Owing to the high degree of control over the dose of Mn^{4+} in $SrAl_2O_4$:Dy^{3+}, diffusing Mn^{4+} into $SrAl_2O_4$:Dy^{3+} provided a unique opportunity to prepare full-color tunable phosphors. This approach could be the basis for convenient color control of Dy^{3+}-doped materials by controlling the red emission intensity of Mn^{4+} in the host.

Supplementary Materials: The following supporting information can be downloaded at: https://www.mdpi.com/article/10.3390/ma15228170/s1. Figure S1. High-resolution XPS spectrum of O 1s in $SrAl_2O_4$:Dy^{3+},Mn^{4+} nanocrystals. Figure S2. PL photograph of $SrAl_2O_4$:Dy^{3+} before Mn^{4+} diffusion. Doping concentration of Dy^{3+} is 1.6 mol% Excitation wavelength is 325 nm. Figure S3. PL spectra of $SrAl_2O_4$:Dy^{3+} after Mn^{4+} diffusion at 800 °C (a), 900 °C (b), and 1000 °C (c) for 4 h. Inset: zoomed section of the PL spectra of $SrAl_2O_4$:Dy^{3+}, Mn^{4+} in the range of 620–700 nm. Figure S4. Normalized dose of Mn^{4+} in $SrAl_2O_4$:Dy^{3+} as a function of diffusion temperature for a given value of E_A. Figure S5. CIE chromaticity diagram of the emissions from $SrAl_2O_4$:Dy^{3+} before Mn^{4+} diffusion (a) and after Mn^{4+} diffusion at 600 °C (b), 700 °C (c), 800 °C (d), 900 °C (e) and 1000 °C (f). The diffusion time is 4 h.

Author Contributions: B.-g.Z. synthesized the materials and wrote the initial drafts. M.M.C. analyzed the data. Y.M.H. designed the experiments and supervised this work. All authors have read and agreed to the published version of the manuscript.

Funding: This research was Financially supported by National Natural Science Foundation of China (no. 11574036).

Institutional Review Board Statement: Not applicable.

Informed Consent Statement: Not applicable.

Data Availability Statement: Data are available upon request.

Acknowledgments: Financial support from National Natural Science Foundation of China (no. 11574036) was acknowledged.

Conflicts of Interest: The authors declare no conflict of interest.

References

1. Shrivastava, R.; Kaur, J.; Dubey, V. White Light Emission by Dy^{3+} Doped Phosphor Matrices: A Short Review. *J. Fluoresc.* **2015**, *26*, 105–111. [CrossRef] [PubMed]
2. Ma, Q.-L.; Zhai, B.-G.; Huang, Y.M. Effect of sol–gel combustion temperature on the luminescent properties of trivalent Dy doped $SrAl_2O_4$. *Ceram. Int.* **2015**, *41*, 5830–5835. [CrossRef]
3. Huang, Y.M.; Ma, Q.-L. Long afterglow of trivalent dysprosium doped strontium aluminate. *J. Lumin.* **2015**, *160*, 271–275. [CrossRef]
4. Zhai, B.-G.; Yang, L.; Ma, Q.-L.; Liu, X.; Huang, Y.M. Mechanism of the prolongation of the green afterglow of $SrAl_2O_4$:Dy^{3+} caused by the use of H_3BO_3 flux. *J. Lumin.* **2017**, *181*, 78–87. [CrossRef]
5. Zhai, B.G.; Huang, Y.M. Green afterglow of undoped $SrAl_2O_4$. *Nanomaterials* **2021**, *11*, 2331. [CrossRef] [PubMed]
6. Shrivastava, R.; Kaur, J.; Dash, M. Studies on white light emission of $Sr_2MgSi_2O_7$ doped with Dy^{3+} phosphors. *Superlattices Microstruct.* **2015**, *82*, 262–268. [CrossRef]
7. Cho, S. Photoluminescence properties of $BaMoO_4$:RE^{3+} (RE = Eu, Sm, Dy, Tb, Tm) phosphors. *J. Korean Phys. Soc.* **2016**, *69*, 1479–1484. [CrossRef]
8. Xiong, F.B.; Han, C.Y.; Lin, H.F.; Wang, Y.P.; Lin, H.Y.; Shen, H.X.; Zhu, W.Z. White light emission from novel host-sensitized single-phase Y_2WO_6:Ln^{3+} (Ln^{3+} = Eu^{3+}, Dy^{3+}) phosphors. *Ceram. Int.* **2016**, *42*, 13841–13848. [CrossRef]
9. Naidu, S.A.; Boudin, S.; Varadaraju, U.; Raveau, B. Host-sensitized emission of $LiInW_2O_8$ wolframites: From red-Eu^{3+} to white-Dy^{3+} phosphors. *J. Solid State Chem.* **2011**, *184*, 2566–2570. [CrossRef]
10. Balakrishna, A.; Ntwaeaborwa, O.M. Study of luminescent behavior and crystal defects of different $MNa[PO_4]$-Dy^{3+} phos-phors (M = Mg, Ca, Sr and Ba). *Sens. Actuat. B* **2017**, *242*, 305–317. [CrossRef]
11. Wu, J.; Zhang, L.; Ben, Y.; Chen, H.; Fu, X.; Wong, C. Improved full-color emission and switched luminescence in single $Ca_3(PO_4)_2$: Dy^{3+}, Eu^{3+} phosphors for white LEDs. *J. Alloy. Compd.* **2017**, *697*, 215–221. [CrossRef]
12. Brik, M.; Srivastava, A. On the optical properties of the Mn^{4+} ion in solids. *J. Lumin.* **2013**, *133*, 69–72. [CrossRef]
13. Li, Y.; Qi, S.; Li, P.; Wang, Z. Research progress of Mn doped phosphors. *RSC Adv.* **2017**, *7*, 38318–38334. [CrossRef]
14. Chi, N.T.K.; Tuan, N.T.; Lien, N.T.K.; Nguyen, D.H. Red Emission of $SrAl_2O_4$:Mn^{4+} Phosphor for Warm White Light-Emitting Diodes. *J. Electron. Mater.* **2018**, *47*, 4571–4578. [CrossRef]
15. Xu, Y.; Wang, D.; Wang, L.; Ding, N.; Shi, M.; Zhong, J.; Qi, S. Preparation and luminescent properties of a new red phosphor ($Sr_4Al_{14}O_{25}$:Mn^{4+}) for white LEDs. *J. Alloy. Compd.* **2012**, *550*, 226–230. [CrossRef]
16. Ye, T.; Li, S.; Wu, X.; Xu, M.; Wei, X.; Wang, K.; Bao, H.; Wang, J.; Chen, J. Sol–gel preparation of efficient red phosphor Mg_2TiO_4:Mn^{4+} and XAFS investigation on the substitution of Mn^{4+} for Ti^{4+}. *J. Mater. Chem. C* **2013**, *1*, 4327–4333. [CrossRef]
17. Medić, M.M.; Brik, M.G.; Dražić, G.; Antić, Z.M.; Lojpur, V.M.; Dramićanin, M.D. Deep-Red Emitting Mn^{4+} Doped Mg_2TiO_4 Nanoparticles. *J. Phys. Chem. C* **2015**, *119*, 724–730. [CrossRef]
18. Murata, T.; Tanoue, T.; Iwasaki, M.; Morinaga, K.; Hase, T. Fluorescence properties of Mn^{4+} in $CaAl_{12}O_{19}$ compounds as red-emitting phosphor for white LED. *J. Lumin.* **2005**, *114*, 207–212. [CrossRef]
19. Cao, R.; Zhang, F.; Cao, C.; Yu, X.; Liang, A.; Guo, S.; Xue, H. Synthesis and luminescence properties of $CaAl_2O_4$:Mn^{4+} phosphor. *Opt. Mater.* **2014**, *38*, 53–56. [CrossRef]
20. Zhai, B.G.; Huang, Y.M. Blue afterglow from undoped $CaAl_2O_4$. *Europhys. Lett.* **2019**, *127*, 17001. [CrossRef]
21. Zhai, B.G.; Ma, Q.L.; Xiong, R.; Li, X.; Huang, Y.M. Blue-green afterglow of $BaAl_2O_4$:Dy^{3+} phosphors. *Mater. Res. Bull.* **2016**, *75*, 1–6. [CrossRef]
22. Shannon, R.D. Revised effective ionic radii and systematic studies of interatomic distances in halides and chaleogenides. *Acta Crystallogr.* **1976**, *32*, 751–767. [CrossRef]
23. Zhai, B.-G.; Xu, H.; Zhuo, F.; Huang, Y.M. Annealing temperature dependent photoluminescence and afterglow of undoped $CaAl_2O_4$. *J. Alloy. Compd.* **2019**, *821*, 153563. [CrossRef]
24. Zhai, B.-G.; Xu, H.; Huang, Y.M. Annealing temperature dependent afterglow of Tb^{3+} doped $CaAl_2O_4$. *Opt. Mater.* **2020**, *112*, 110739. [CrossRef]
25. Zhai, B.-G.; Huang, Y.M. Green photoluminescence and afterglow of Tb-doped $SrAl_2O_4$. *J. Mater. Sci.* **2016**, *52*, 1813–1822. [CrossRef]
26. De Biasi, R.S.; Grillo, M.L.N. Investigation of Mn^{2+} diffusion in lime (CaO) using electron magnetic resonance. *Mater. Res.* **2014**, *17*, 434–435. [CrossRef]
27. Portavoce, A.; Abbes, O.; Rudzevich, Y.; Chow, L.; le Thanh, V.; Girardeaux, C. Manganese diffusion in monocrystalline germanium. *Scr. Mater.* **2012**, *67*, 269–272. [CrossRef]
28. Kumar, V.; Pandey, A.; Ntwaeaborwa, O.M.; Dutta, V.; Swart, H.C. Structural and luminescence properties of Eu^{3+}/Dy^{3+} embedded sodium silicate glass for multicolour emission. *J. Alloys Compd.* **2017**, *708*, 922–931. [CrossRef]

29. Li, X.; Wang, X.; Li, X.; Cheng, L.; Tong, L.; Wang, W.; Sun, J.; Zhang, J.; Chen, B. Luminescence studies of Sm^{3+} single-doped and Sm^{3+}, Dy^{3+} co-doped $NaGdTiO_4$ phosphors. *Phys. B Condens. Matter* **2016**, *481*, 197–203. [CrossRef]
30. Pawar, P.P.; Munishwar, S.R.; Gedam, R.S. Physical and optical properties of Dy^{3+}/Pr^{3+} co-doped lithium borate glasses for W-LED. *J. Alloy. Compd.* **2016**, *660*, 347–355. [CrossRef]
31. Ma, Q.-L.; Xiong, R.; Huang, Y.M. Tunable photoluminescence of porous silicon by liquid crystal infiltration. *J. Lumin.* **2011**, *131*, 2053–2057. [CrossRef]
32. Ma, Q.-L.; Zhai, B.-G.; Huang, Y.M. Sol–gel derived ZnO/porous silicon composites for tunable photoluminescence. *J. Sol-Gel Sci. Technol.* **2012**, *64*, 110–116. [CrossRef]
33. Sun, Q.; Wang, S.; Devakumar, B.; Sun, L.; Liang, J.; Huang, X. Synthesis, crystal structure, and photoluminescence characteris-tics of high–efficiency deep–red emitting Ba_2GdTaO_6:Mn^{4+} phosphors. *ACS Omega* **2019**, *4*, 13474–13480. [CrossRef] [PubMed]
34. Senden, T.; Van Dijk-Moes, R.J.A.; Meijerink, A. Quenching of the red Mn^{4+} luminescence in Mn^{4+}-doped fluoride LED phosphors. *Light Sci. Appl.* **2018**, *7*, 8. [CrossRef] [PubMed]
35. Li, K.; Lian, H.; van Deun, R. Site occupancy and photoluminescence properties of a novel deep-redemitting phosphor $NaMgGdTeO_6$:Mn^{4+} with perovskite structure for w-LEDs. *J. Lumin.* **2018**, *198*, 155–162. [CrossRef]
36. Jara, E.; Valiente, R.; Bettinelli, M.; Rodríguez, F. Understanding the efficiency of Mn^{4+} phosphors: Study of the spinel $Mg_2Ti_{1-x}Mn_xO_4$. *J. Phys. Chem. C* **2021**, *125*, 27118–27129. [CrossRef]
37. Babin, V.; Bohacek, P.; Bender, E.; Krasnikov, A.; Mihokova, E.; Nikl, M.; Senguttuvan, N.; Stolovits, A.; Usuki, Y.; Zazubovich, S. Decay kinetics of the green emission in tungstates and molybdates. *Radiat. Meas.* **2004**, *38*, 533–537. [CrossRef]
38. Zhai, B.G.; Yang, L.; Zhou, F.F.; Shi, J.S.; Huang, Y.M. Strong photo-oxidative capability of $ZnWO_4$ nanoplates with highly exposed {0-11} facets. *Catalysts* **2019**, *9*, 178. [CrossRef]
39. Huang, Y.M.; Li, M.Y.; Yang, L.; Zhai, B.G. Eu^{2+} and Eu^{3+} doubly doped $ZnWO_4$ nanoplates with superior photocatalytic per-formance for dye degradation. *Nanomaterials* **2018**, *8*, 765. [CrossRef]
40. Zhai, B.-G.; Ma, Q.-L.; Yang, L.; Huang, Y.M. Growth of $ZnMoO_4$ nanowires via vapor deposition in air. *Mater. Lett.* **2017**, *188*, 119–122. [CrossRef]
41. Zhai, B.-G.; Ma, Q.-L.; Yang, L.; Huang, Y.M. Effects of Sintering Temperature on the Morphology and Photoluminescence of Eu^{3+} Doped Zinc Molybdenum Oxide Hydrate. *J. Nanomater.* **2018**, *2018*, 7418508. [CrossRef]
42. Zhai, B.-G.; Ma, Q.-L.; Yang, L.; Huang, Y.M. Synthesis and optical properties of Tb-doped pentazinc dimolybdate pentahydrate. *Results Phys.* **2017**, *7*, 3991–4000. [CrossRef]
43. Zhai, B.G.; Yang, L.; Huang, Y.M. Intrinsic defect engineering in Eu^{3+} doped $ZnWO_4$ for annealing temperature tunable photoluminescence. *Nanomaterials* **2019**, *9*, 99. [CrossRef] [PubMed]